AMERICAN ACADEMY OF OPHTHALMOLOGY®

Multimodal Imaging of Fundus Abnormalities in Stickler Syndrome: Characterization of 15 Distinct Features Using Ultra-Widefield Swept-Source OCT Angiography

Yarou Hu, PhD,[1,] Kaixuan Cui, PhD,[1,2,*] Zhenquan Wu, PhD,[1,2,*] Jiani Li, PhD,[2] Sihui Zhang, PhD,[2] Xiayuan Luo, MSc,[2] Honghui He, BSN,[2] Xiaorong Cheng, BSN,[2] Guishuang Ying, PhD,[3] Xinyu Zhao, PhD,[1,2,†] Guoming Zhang, PhD[1,2,†]*

Purpose: To roundly characterize fundus features of Stickler syndrome using multimodal imaging and address the gap in imaging evidence for retinal detachment (RD).

Design: A cohort study.

Participants: This study included 25 eyes from 13 patients with Stickler syndrome at an outpatient clinic between January 2025 and January 2026.

Methods: Basic data were collected using cycloplegic refraction and IOLMaster 700, and multimodal imaging was performed using scanning laser ophthalmoscopy and ultra-widefield (UWF) swept-source (SS) OCT angiography (OCTA).

Main Outcome Measures: Three ophthalmologists independently documented and then consolidated the manifestations and detection rate of all fundus abnormalities. Statistical analysis was performed using SPSS 27.0.

Results: Among patients, 15 distinct features were identified, and most had detection rates >50%. Vitreous abnormalities were most common: opacities (100%), liquefaction pockets (92%), lamellation (92%), and punctate dense granules (92%). Most vitreoretinal and retinal features had detection rates >75%, whereas intraretinal cystoid spaces (50%), retinal breaks (33%), and RD (8%) were lower, likely because of the young age. Detection rates of foveal hypoplasia (FH) (75%), foveal avascular zone (FAZ) absence (46%), and fingerprint sign (17%) decreased sequentially. Pitted retinal surface ($P = 0.04$) and RD ($P = 0.008$) were significantly positively correlated with AL. The fundus features exhibit age-related trends and a tendency for internal correlation. Moreover, vitreous lamellation and liquefaction pockets ($P < 0.05$), vitreous anchoring and vitreoretinal traction ($P < 0.05$), and FAZ presence and FH ($P < 0.01$) showed significant correlations.

Conclusions: This study used UWF SS-OCTA to systematically characterize fundus phenotypes of Stickler syndrome. Among the 15 identified features, vitreous abnormalities were the most prevalent. We provide in vivo imaging evidence that vitreous anchoring may be a key trigger for retinal breaks and detachment in Stickler syndrome, likely acting through vitreoretinal traction. Its concealment beneath the vitreous fibrous strands may offer a potential theoretical basis for improving targeted prophylaxis and treatment. The other features, such as pitted retinal surface and FH-related macular signs, may serve as imaging biomarkers, aiding early and efficient diagnosis or risk stratification.

Financial Disclosure(s): The authors have no proprietary or commercial interest in any materials discussed in this article. *Ophthalmology Science 2026;6:101397* *© 2026 American Academy of Ophthalmology, Inc. Published by Elsevier Inc. This is an open access article under the CC BY-NC-ND license (http://creativecommons.org/licenses/by-nc-nd/4.0/).*

Supplemental material available at www.ophthalmologyscience.org.

Stickler syndrome, also known as hereditary progressive arthro-ophthalmopathy, is a common hereditary connective tissue disorder, with an estimated incidence of 1 in 7500 to 1 in 9000.[1] It is a multisystem condition involving the auditory system, craniofacial region, skeleton, joints, and eyes.[2] Among its various phenotypes, ocular involvement is particularly prominent because of its unpredictable progression; notably, retinal detachment (RD) may occur even after prophylactic treatment, posing a high risk of visual impairment and blindness.[3] In contrast, the nonocular manifestations can be alleviated with appropriate therapies or remain relatively stable, with limited impact on daily functioning.[4] Moreover, the complexity of fundus abnormalities increases surgical

© 2026 American Academy of Ophthalmology, Inc
Published by Elsevier Inc. This is an open access article under the CC BY-NC-ND license (http://creativecommons.org/licenses/by-nc-nd/4.0/).
http://doi.org/10.1016/j.xops.2026.101397
ISSN 2666-9145/26

difficulty and contributes to a high risk of postoperative recurrence, making ocular management a central challenge in the clinical care of this disease.[5,6]

Stickler syndrome is the most common cause of hereditary RD in children.[7] Previous studies have proposed different mechanisms underlying RD. Some investigators have suggested that posterior vitreous detachment is the primary risk factor,[8,9] whereas others emphasize the role of intrinsic vitreous abnormalities and retinal thinning associated with perivascular or peripheral retinal degeneration.[10] However, the former hypothesis does not adequately explain the high incidence of RD in young patients who have not yet developed posterior vitreous detachment.[11] Conversely, the latter is limited by a lack of direct imaging evidence for the interplay of abnormal adhesion and traction between the vitreous and retina. Consequently, the exact pathologic mechanism underlying RD in Stickler syndrome remains incompletely understood, thereby hindering the development of early intervention strategies.

Currently, the diagnosis of Stickler syndrome relies primarily on clinical manifestations and genetic testing, particularly the latter. Although scanning laser ophthalmoscopy (SLO) enables visualization of nearly the entire fundus, the identification of precise imaging biomarkers remains limited, constraining advances in diagnostic methods. In recent years, the emergence of ultra-widefield (UWF) swept-source (SS) OCT angiography (OCTA) has not only enabled wide-field, high-resolution imaging but has also improved visualization of the vitreous body,[12] an area that has previously lacked effective in vivo assessment tools in Stickler syndrome.

To better elucidate the mechanism of RD in Stickler syndrome and address gaps in fundus imaging data, we performed comprehensive in vivo retinal imaging using UWF SS-OCTA. This approach provided direct imaging evidence of vitreoretinal traction and resultant retinal breaks. In addition, we systematically identified a series of novel fundus features of Stickler syndrome and comprehensively characterized its fundus phenotypic spectrum.

Methods

This is a cohort study conducted at Shenzhen Eye Hospital. The study protocol was approved by the Medical Ethics Committee of Shenzhen Eye Hospital (2025KYPJ208), and informed consent was obtained from the parents or legal guardians of all participants before study initiation. This study adhered to the Declaration of Helsinki.

Patient Enrollment

Since 2004, our research team has managed patients through the Eyecare-cloud platform.[13] This longitudinal cohort database includes hundreds of families affected by inherited eye diseases, and all patients enrolled in this study were registered in and uniformly managed through this platform. We included all patients diagnosed with Stickler syndrome who visited our outpatient clinic between January 2025 and January 2026 and had complete information recorded through the platform.

The inclusion criteria were as follows: (1) diagnosis of Stickler syndrome based on comprehensive ophthalmic examinations, medical history (including medical records, systemic examination reports, and treatment histories for systemic diseases from general hospitals), and genetic testing results; and (2) age >18 years. The exclusion criteria were as follows: (1) inability to undergo fundus imaging because of a history of ocular surgery (such as vitrectomy), ocular trauma (such as penetrating eye injury), refractive media opacities (such as corneal disease and cataract), or disorganized structures of the fundus (such as proliferative vitreoretinopathy and phthisis bulbi); and (2) inability to cooperate with the examinations because of comorbid psychiatric disorders, or marked nystagmus.

On the same day of the study visit, all patients underwent the measurement of cycloplegic refraction and ocular biometry to collect basic clinical data, along with comprehensive fundus examinations for the acquisition of multimodal images. All examinations were performed by experienced, certified examiners following standardized protocols. The clinical data and images were independently reviewed and analyzed by 2 fundus ophthalmologists. Final adjudication was performed by a senior ophthalmologist (G.Z.) with >20 years of clinical experience in pediatric fundus diseases to ensure accuracy of measurements, optimal image quality, and consistency in lesion identification and classification (Fig S1, available at www.ophthalmologyscience.org).

Basic Clinical Data Acquisition

Refraction measurements were performed by a certified optometrist with >15 years of experience in pediatric optometry. Cycloplegia was induced using 0.5% compound tropicamide eye drops (administered once every 5−10 minutes for a total of 3 times). Once the pupils were dilated to 6 mm in diameter, retinoscopy was performed under dark-room conditions. After determination of the final refraction, the spherical equivalent was calculated as sphere plus one-half of the cylinder power.

The ocular biometry was performed using the IOLMaster 700 (Carl Zeiss Meditec AG), with primary measurement of axial length (AL). Axial length, together with the refractive error, was recorded as key baseline clinical data, given the high prevalence of myopia among patients with Stickler syndrome.

Multimodal Image Acquisition

Multimodal images comprised 4 modalities: color fundus images acquired by SLO (Optos 200Tx, Optos PLC), as well as the transverse scan images, blood flow images, and en face images of different capillary plexuses, acquired by UWF SS-OCTA (BM-400K BMizar, TowardPi Medical Technology).

Scanning laser ophthalmoscopy was used to sequentially acquire fundus images in the central, superior, nasal, inferior, and temporal fields for all patients, ensuring near-complete retinal coverage. This approach enabled comprehensive assessment of the fundus features, including vitreous morphology, retinal degeneration, and macular foveal reflex. Scanning laser ophthalmoscopy is a clinically accessible imaging technique for documenting fundus characteristics. In this study, we compared SLO with UWF SS-OCTA to evaluate their relative utility and identify a more suitable imaging approach for detailed fundus assessment.

Ultra-widefield SS-OCTA enables simultaneous acquisition of the 3 aforementioned imaging modalities within a single scan. The system performs high-density, continuous, full-layer scanning over an approximately 20 × 24 mm^2 retinal area without the need for image stitching, generating up to 1280 sections and a scan depth up to 6 mm. This allows clear visualization of both the retina and the posterior vitreous. Ultra-widefield SS-OCTA also provides

rapid image acquisition (as fast as 15 seconds) and high resolution (transverse resolution up to 3.8 μm), along with automated segmentation and quantitative analysis capabilities. In this study, central-view fundus imaging was first performed using UWF SS-OCTA to capture the posterior pole, midperiphery, and portions of the peripheral retina. Targeted, continuous scans of peripheral areas with suspected lesions were then obtained by guiding patients through controlled ocular rotations, ensuring comprehensive detection of fundus abnormalities in each patient.

Based on the multimodal images captured by UWF SS-OCTA, we systematically summarized all identified abnormal fundus findings and classified them into 3 major categories according to their anatomic structures, which were further subdivided into 15 features (4 vitreous, 3 vitreoretinal, 5 retinal, and 3 macular features) according to their morphologic manifestations. Definitions of the 15 fundus features are shown in Table S1 (available at www.ophthalmologyscience.org). This classification is not intended to establish new definitions of the lesions but rather to provide a more accurate and intuitive representation of our findings. Detection rates for each were calculated among all enrolled patients or eyes. For specific features, cases were excluded from the calculation when the feature could not be reliably assessed, such as when peripheral imaging was difficult to obtain or when images were unavailable.

Statistical Analysis

The statistical analyses were performed using SPSS 27.0 (SPSS, Inc). Descriptive analyses were performed using mean ± standard deviation for continuous measures, count, and percentages for categorical measures. Point-biserial correlation was used to analyze the correlation between normally distributed continuous and categorical variables, whereas Spearman rank-order correlation was used for nonnormally distributed continuous data and categorical data. Φ Coefficient was used for the correlation analysis between categorical variables.

Results

Baseline and Fundus Features

A total of 25 eyes from 13 enrolled patients with Stickler syndrome underwent multimodal imaging examination and characterization. One eye was excluded because of phthisis bulbi resulting from long-standing RD. The vast majority of the patients carried COL2A1 mutations (type 1), whereas only 1 patient harbored a COL11A1 mutation (type 2), and no discernible phenotypic differences in fundus manifestations were observed in this isolated case compared with the others. All patients were children, with a mean age of 7.3 years and a nearly equal gender distribution (6 women and 7 men). Their basic refractive characteristics, including spherical equivalent and AL, were −11.6 ± 6.5 diopters and 27.5 ± 1.8 mm, respectively (Table 1).

The 15 distinct features we identified with their detection rates are shown in Table 1, most of which had detection rates >50%. The 4 vitreous features were the most predominant: vitreous liquefaction pockets (92%; bilateral, 62%), vitreous lamellation (92%; bilateral, 69%), vitreous opacities (100%; bilateral, 100%), and punctate dense granules (92%; bilateral, 83%). Most vitreoretinal and retinal features were also common, with vitreous anchoring, vitreoretinal traction, retinal degeneration, pitted retinal surface, and perivascular cavitation with inner retinal atrophy (PCIRA) detected in 92%, 75%, 100%, 75%, and 90% of patients, respectively; whereas the other retinal features—intraretinal cystoid spaces (50%), retinal breaks (33%), and RD (8%)—were relatively lower. The detection rates of the macular features, including foveal hypoplasia (FH), foveal avascular zone (FAZ) absence, and fingerprint sign, were decreased sequentially by 75%, 46%, and 17%, respectively.

Imaging Manifestations of Fundus Features

Figure 1 comprises navigation and transverse scan images from superior to inferior of the fundus in a patient with Stickler syndrome, demonstrating all 4 vitreous features, in order: vitreous liquefaction pocket, vitreous lamellation, vitreous opacities, and punctate dense granules. Notably, vitreous liquefaction appears to occur in the central vitreous (Fig 1D), without typical posterior vitreous detachment—or presenting only as localized, partial posterior vitreous detachment—as residual vitreous remains adherent to the retinal surface (Fig 1F). The partial posterior vitreous detachment may give rise to the lamellar vitreous remaining on the retinal surface (Fig 1E), which tapers gradually from the peripheral retina toward the posterior pole. In addition, a dense reflective band is visible anterior to the lamellar vitreous (Fig 1K). Vitreous opacities are typically accompanied by shadowing artifacts beneath the opacities (Fig 1F), whereas punctate dense granules usually do not produce such artifacts (Fig 1J).

Typical vitreoretinal features and their resultant complications are shown in Figure 2. Vitreous anchoring can be seen in Figure 2D–F, as well as in Figure 1L, and may coexist with or be independent of retinal degenerative areas. As demonstrated in Figure 2J–L, vitreous anchoring could lead to secondary vitreoretinal traction, and such traction can result in the development of intraretinal cystoid changes, lamellar or full-thickness retinal breaks, and RD. The features of retinal degeneration are highly diverse, which can present as any of the vitreoretinal and retinal features described in this study (Figs 2–4). Additional manifestations of retinal degeneration are shown in Figure S2 (available at www.ophthalmologyscience.org).

The retinal features are presented in Figures 3 and 4. A pitted retinal surface is observed in the midperipheral and peripheral retina, without obvious vitreous adhesion or traction on the retinal surface (Fig 3D–F). Perivascular cavitation with inner retinal atrophy is commonly found around the major retinal vascular trunks and their main branches (Fig 3J–L). Intraretinal cystoid spaces can be observed adjacent to retinal vessels or within areas of peripheral retinal degeneration. Compared with perivascular cavitation in PCIRA, they tend to be larger in size and may represent progressive changes of the former (Fig 4D–F). Lamellar or full-thickness retinal breaks were found adjacent to PCIRA (Figs 4J, and 5E, J, O), as well as detected in

Table 1. Clinical Characteristics of the Patients with Stickler Syndrome

Clinical Characteristics	Patients (N = 13)		Eyes (N = 25)
	*Unilateral Eye**	*Bilateral Eyes*†	
Age (yr)	7.3 ± 3.2		7.0 ± 2.6
Gender (female/male)	6/7		12/13
SE (D)	NA		−11.6 ± 6.5
AL (mm)	NA		27.5 ± 1.8
Vitreous features (*n*/*N*, %)			
Vitreous liquefaction pockets	12/13 (92%)	8/13 (62%)	19/25 (76%)
Vitreous lamellation	12/13 (92%)	9/13 (69%)	20/25 (80%)
Vitreous opacities	13/13 (100%)	13/13 (100%)	25/25 (100%)
Punctate dense granules	11/12 (92%)	10/12 (83%)	19/22 (86%)
Vitreoretinal features (*n*/*N*, %)			
Vitreous anchoring	11/12 (92%)	10/12 (83%)	19/22 (86%)
Vitreoretinal traction	9/12 (75%)	6/12 (50%)	14/23 (61%)
Retinal degeneration	12/12 (100%)	11/12 (92%)	22/23 (96%)
Retinal features (*n*/*N*, %)			
Pitted retinal surface	9/12 (75%)	8/12 (67%)	16/23 (70%)
PCIRA	9/10 (90%)	8/10 (80%)	17/20 (85%)
Intraretinal cystoid spaces	6/12 (50%)	3/12 (25%)	7/22 (32%)
Retinal breaks	4/12 (33%)	0/12 (0%)	4/23 (17%)
RD	1/13 (8%)	0/13 (0%)	1/25 (4%)
Macular features (*n*/*N*, %)			
FH	9/12 (75%)	9/12 (75%)	18/24 (75%)
FAZ absence	5/11 (46%)	5/12 (42%)	10/22 (46%)
Fingerprint sign	2/12 (17%)	1/12 (8%)	3/24 (13%)

AL = axial length; D = diopter; FAZ = foveal avascular zone; FH = foveal hypoplasia; NA = not available; PCIRA = perivascular cavitation with inner retinal atrophy; RD = retinal detachment; SE = spherical equivalent.
*Patients with involvement in at least 1 eye.
†Patients with involvement in both eyes.

the field of vitreous anchoring, vitreoretinal traction, and retinal degeneration, potentially leading to rhegmatogenous RD (Figs 2K, L, and 4K, L).

Figure 5 demonstrates the multimodal features of vitreous anchoring, vitreoretinal traction, pitted retinal surface, PCIRA, and intraretinal cystoid spaces. In the first row, vitreous anchoring is concealed beneath cordlike or beaded vitreous fiber bundles on SLO images, with no abnormalities on blood flow and en face images. The second row shows vitreoretinal traction and retinal break resulting from vitreous anchoring. In the third row, pitted retinal surface appears nearly normal on SLO and blood flow images, whereas en face image reveals distinct craterlike changes resembling the moon surface, confirmed by transverse scan images. As shown in the last 2 rows, when the perivascular features are small or inconspicuous (in a tessellated fundus) on SLO images and mild abnormal on blood flow images, en face images consistently delineate the full contour of the lesions with clarity. Besides, pixel intensity (shades of gray) helps assess retinal thickness and identify retinal breaks. Transverse scan images clearly show intraretinal cystoid spaces, helping determine their extent and severity, whereas en face images only reveal irregular pixel distribution.

Each row in Figure 6 displays multimodal images of the macular region for 1 eye. In the first column, it is evident that all eyes exhibit FH to varying degrees, with the inferiormost eye being the most severely affected. Similarly, in the second column, the FAZs in the third and fourth rows are markedly smaller compared with those in the first and second rows. However, in the fourth column, a distinct gradient of increasingly delayed foveal development is discernible on the en face images of the deep capillary plexus from the first to fourth rows, characterized by a progressively more prominent fingerprint sign. Conversely, in the last column, the macular appearance in the first and second rows appears even worse than that in the third and fourth rows because the latter exhibit foveal reflexes on SLO images.

Correlation Analysis of Fundus Features

Punctate dense granules, vitreous anchoring, pitted retinal surface, PCIRA, and FAZ absence showed significant correlations with age. Additionally, vitreoretinal traction ($\rho = 0.41$; $P = 0.054$) and intraretinal cystoid spaces ($\rho = 0.42$; $P = 0.054$) possibly exhibited similar trends. This suggests that with increasing age, the incidence of certain fundus features in patients' eyes gradually rises. Pitted retinal surface ($\rho = 0.44$; $P = 0.04$) and RD ($\rho = 0.54$; $P = 0.008$) were significantly positively correlated with AL, indicating that as AL increases, the retinal surface becomes uneven and pitted, and the risk of RD also increases. This latter finding is consistent with our current understanding that increased AL, rather than simply an increase in the power of refraction (spherical equivalent), is associated with RD (Table 2).

Figure S3 (available at www.ophthalmologyscience.org) illustrates the pairwise correlations among fundus features in patients with Stickler syndrome. Correlation analysis within each category of the features mainly showed that vitreous lamellation was positively correlated with both vitreous liquefaction pockets ($\rho = 0.42$; $P < 0.05$) and punctate dense granules ($\rho = 0.50$; $P < 0.05$); vitreous anchoring was positively correlated with vitreoretinal traction ($\rho = 0.48$; $P < 0.05$); and the presence of FAZ was significantly negatively correlated with FH ($\rho = -0.56$; $P < 0.01$). Vitreous features (punctate dense granules and vitreous lamellation) showed significant correlations with certain vitreoretinal features (vitreous anchoring and vitreoretinal traction) and some retinal features (PCIRA and pitted retinal surface) ($P < 0.05$). Vitreoretinal features (retinal degeneration and vitreous anchoring) also exhibited significant correlations with some retinal features (PCIRA and pitted retinal surface) ($P < 0.05$). It is noteworthy that the results demonstrate that vitreous anchoring may lead to vitreoretinal traction, which is a significant risk factor for RD, whereas the underlying cause of vitreous anchoring is abnormal

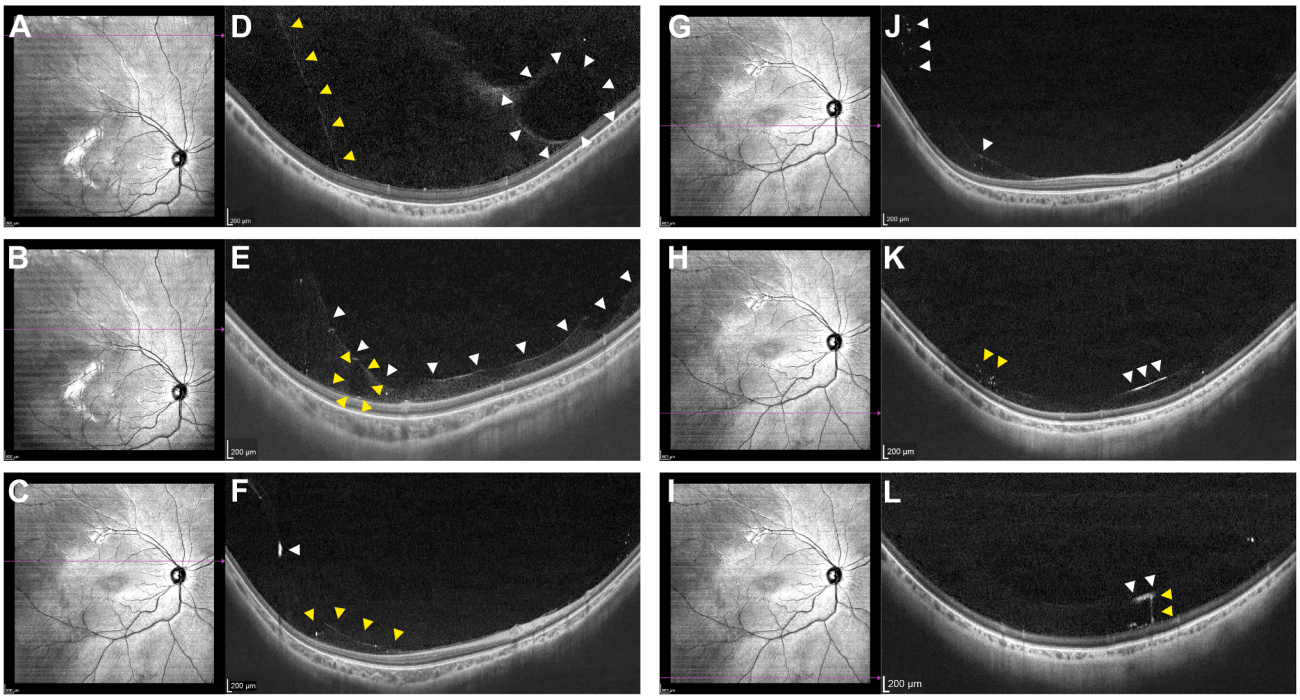


Figure 1. Vitreous features in a patient with Stickler syndrome. **A**–**C** and **G**–**I**, Navigation images of the retinas, with purple transverse lines showing the scan positions. **D**–**F** and **J**–**L**, Transverse scan images from superior to inferior of the fundus. **D**, Representative image of partial posterior vitreous detachment (yellow arrowheads) and vitreous liquefaction. A roundish liquefaction pocket is indicated, with its boundary being relatively denser (white arrowheads). **E**, Representative image of vitreous lamellation (white arrowheads) and small liquefaction pocket within the vitreous lamellation (yellow arrowheads). The vitreous lamellation gradually thins from the peripheral retina to the posterior pole (**D**–**F**, **J**–**L**). **F**, Representative image of vitreous opacity (white arrowhead) and residual vitreous on the retinal surface (yellow arrowheads). **J**, Representative image of punctate dense granules (white arrowheads). **K**, Representative image demonstrating a dense reflective band on the surface of vitreous lamellation (white arrowheads) and punctate dense granules (yellow arrowheads). **L**, Representative image showing vitreous fiber strand opacity (white arrowheads), with vitreous anchoring (yellow arrowheads) visible beneath and connecting to the retinal surface.

morphologic changes of the vitreous body (vitreous lamellation and punctate dense granules).

Discussion

In this multimodal imaging study of fundus abnormalities in patients with Stickler syndrome, we identified 15 fundus features, with majority detected in more than half of the patients with Stickler syndrome. Vitreous features were the most prominent, with all 4 signs observed in >90% of patients, whereas certain vitreoretinal and retinal features also exhibited detection rates >90%. It is worth noting that because of the relatively young age (mean age, 7.3 years) of the patients included in this study, the detection rate of RD was markedly lower than the rates (28%–47%) reported in previous studies.[14,15] However, during our subsequent follow-up, these rates continued to increase (tripled in just a few months), and other features (such as punctate dense granules, vitreous anchoring, and pitted retinal surface) also exhibited significant correlations with age ($P < 0.05$).

To further elucidate the specificity of the fundus features identified in our Stickler syndrome cohort, we compared our findings with those of a study that used SLO and SS-OCT in 1966 myopic eyes.[16] In this comparison, we identified many distinct features, including vitreous anchoring, pitted retinal surface, and PCIRA, suggesting their potential specificity for Stickler syndrome because they have not been observed in eyes with simple myopia. In contrast, for the other features detected by UWF SS-OCTA, such as vitreous liquefaction pockets, vitreous opacities, and other vitreoretinal interface abnormalities within retinal degenerative areas (Fig S2), we have not yet found them to exhibit additional abnormal manifestations that could aid in differentiating eyes affected with Stickler syndrome from simple myopic eyes.

As shown in Figure 1, we observed that vitreous liquefaction in patients with Stickler syndrome occurs as early as childhood (almost all patients aged 4–10 years). At this stage, patients may not develop typical posterior vitreous detachment or may present only with partial posterior vitreous detachment. Residual vitreous remains on the retinal surface and appears as lamellar vitreous, a residual structure following central vitreous liquefaction. Previous case reports have also described vitreous features of patients with Stickler syndrome such as "vitreoschisis with the posterior vitreous cortex splitting into 2 layers"[17] and "partial perifoveal vitreous separation,"[18] both of which also suggest incomplete vitreous detachment, echoing our findings. Additionally,

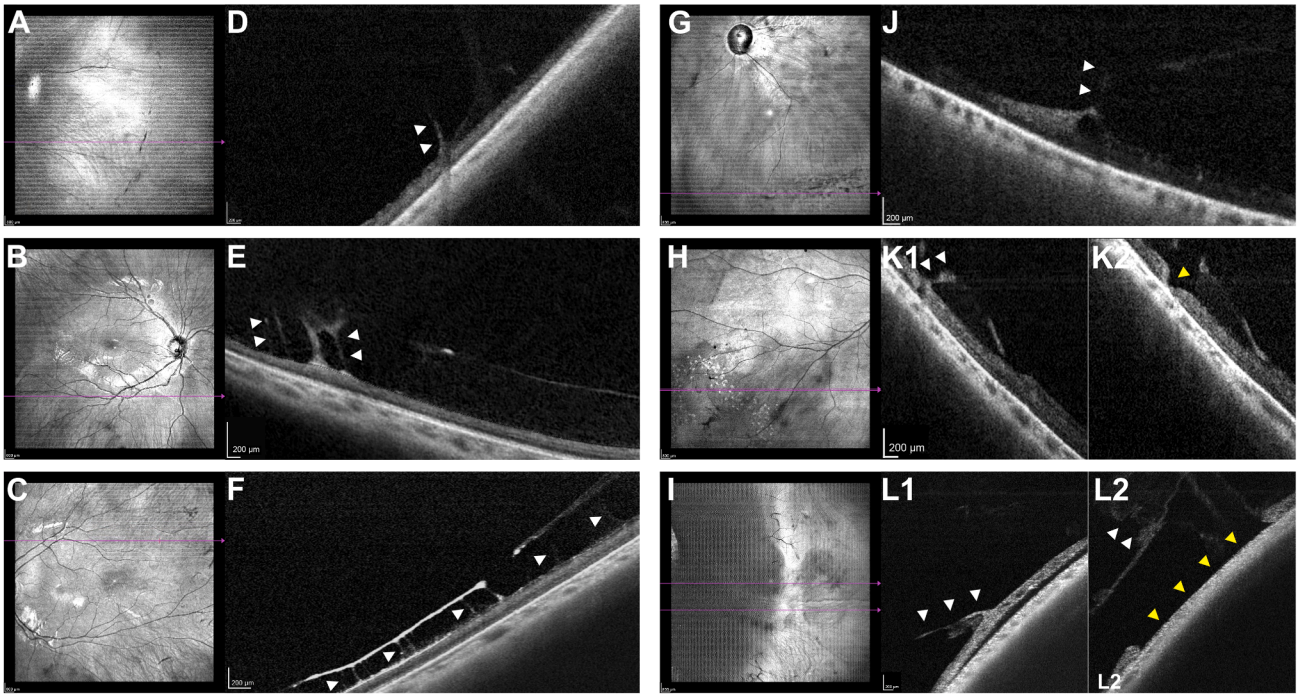


Figure 2. Vitreoretinal features in patients with Stickler syndrome. **A**–**C** and **G**–**I**, Navigation images of the retinas, with purple transverse lines showing the scan positions. **D**–**F**, Transverse scan images of vitreous anchoring (white arrowheads). **J**–**L**, Transverse scan images of vitreoretinal traction that may result from vitreous anchoring (white arrowheads), with retinal breaks (yellow arrowheads).

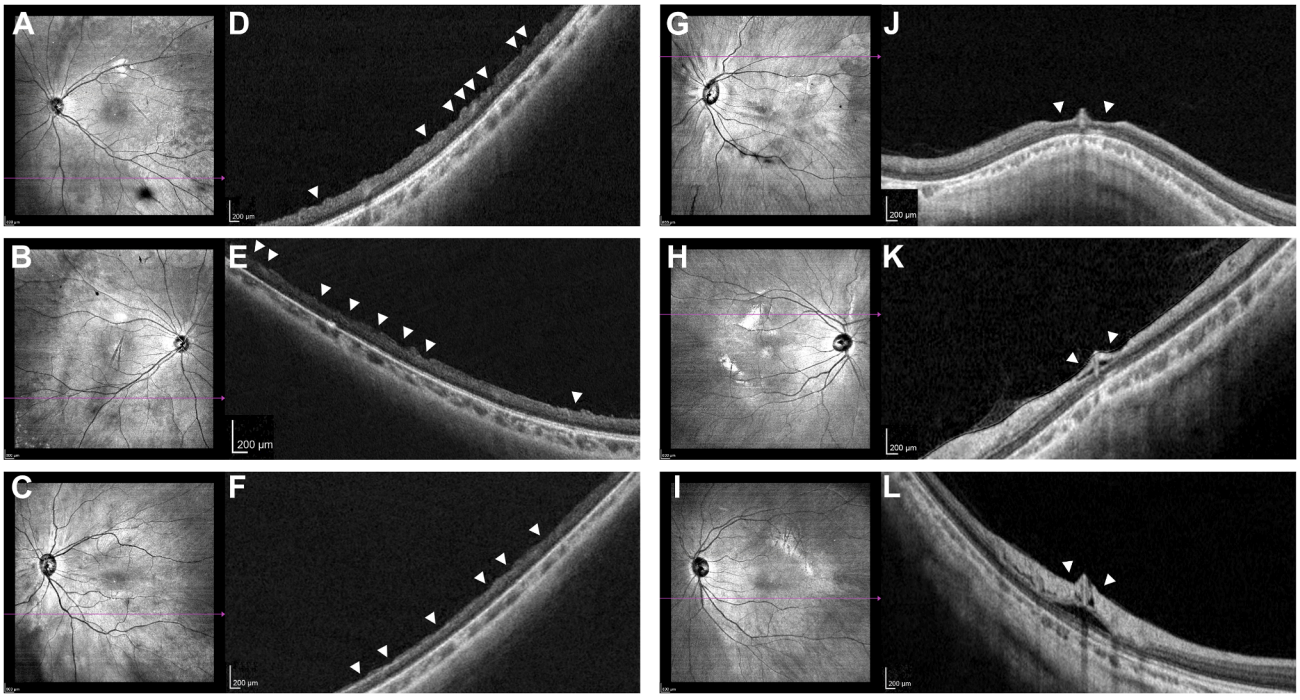


Figure 3. Retinal surface and perivascular features in patients with Stickler syndrome. **A**–**C** and **G**–**I**, Navigation images of the retinas, with purple transverse lines showing the scan positions. **D**–**F**, Transverse scan images of pitted retinal surfaces. The moonlike retinal surface exhibiting an undulating, wavelike appearance on transverse scan images (the small pits/depressions marked by white arrowheads). **J**–**L**, Transverse scan images of perivascular cavitation (**K**, **L**) with inner retinal atrophy (**J**) (white arrowheads).

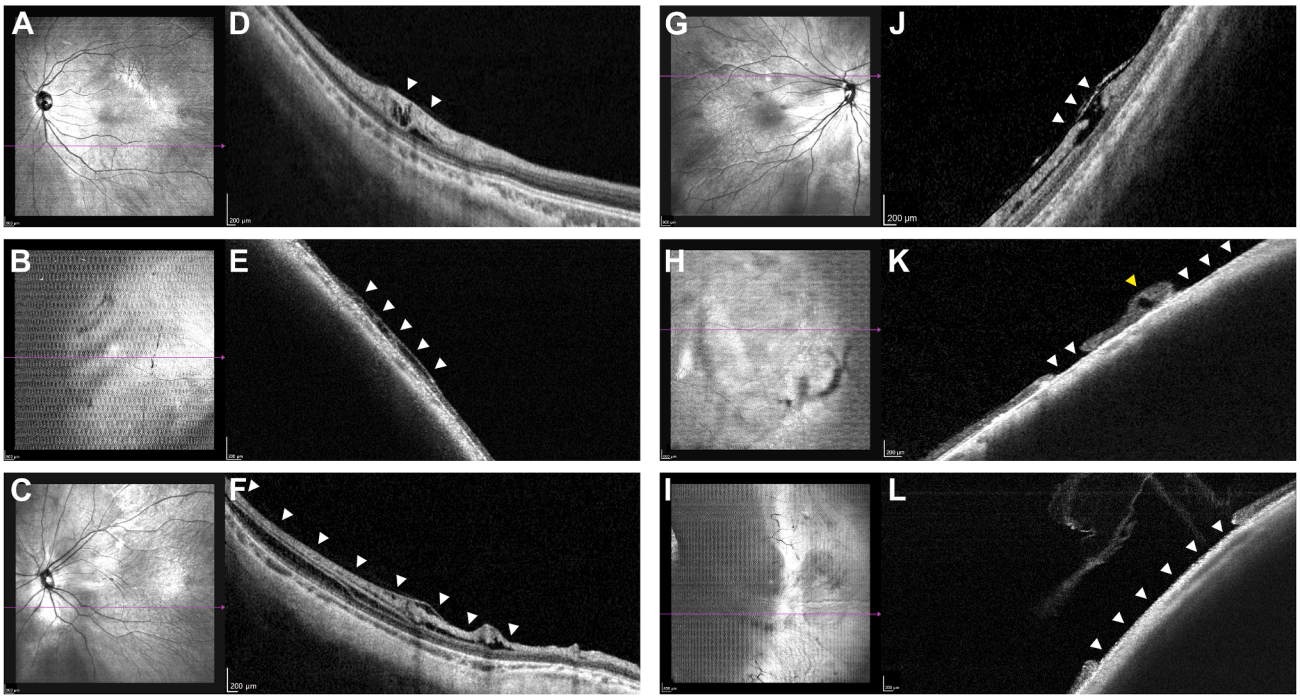


Figure 4. Intraretinal features in patients with Stickler syndrome. **A**–**C** and **G**–**I**, Navigation images of the retinas, with purple transverse lines showing the scan positions. **D**–**F**, Transverse scan images of intraretinal cystoid spaces (white arrowheads). **J**–**L**, Transverse scan images of retinal breaks (white arrowheads), with a retinal cystic cavity (**K**) (yellow arrowheads).

one of the reports described the feature of "perimacular cisterns within formed cortical vitreous."[18] Upon comparison, we found that this finding essentially corresponds to the "small liquefaction pocket within the vitreous lamellation" shown in Figure 1E, except that they referred to the preretinal vitreous lamellation as "cortical vitreous." The vitreous lamellation may represent residual vitreous structure after the liquefaction and collapse of gel in the vitreous cavity ($\rho = 0.42$; $P = 0.04$), which may result from vitreous compartmentalization driven by genetic regulation or the developmental environment.[19] These findings suggest that the previous view attributing RD in Stickler syndrome to posterior vitreous detachment may be overly simplistic.[9,20]

It is well known that vitreous liquefaction, retinal traction, and full-thickness retinal breaks constitute 3 elements of rhegmatogenous RD.[21] This study not only confirms the presence of vitreous liquefaction but also provides in vivo imaging evidence of retinal breaks potentially caused by vitreoretinal traction secondary to vitreous anchoring, which typically presents as single or multiple firm, linear vitreous strands that are vertically oriented and adherent to the retinal surface (Fig 2). This finding echoes the report by MacRae et al,[22] which described abnormal connections formed by vitreous collagen incarcerated within the inner retinal surface in an enucleated globe from a patient with Stickler syndrome. Correlation analysis in this study also indicates that there was a significant positive correlation between vitreous anchoring and vitreoretinal traction ($\rho = 0.48$; $P = 0.03$). Given the aforementioned findings, we propose a new supplementary explanation for RD in young patients: vitreous anchoring could be an important initiating factor, and its resultant traction may serve as key for the development of retinal breaks and detachment.

Although some studies have noted the role of abnormal vitreous and perivascular lattice degeneration in RD in Stickler syndrome,[10] our study differs in that we suggest that vitreoretinal traction is not confined to degenerative areas. Moreover, in our imaging of perivascular lesions (Fig 3), typical signs such as vitreoretinal traction and white-sheathed vessels were rarely observed, raising our questions about the accuracy of the use of "lattice."[8,23] Therefore, we renamed perivascular lattice according to its actual OCT appearance as "PCIRA." The perivascular lesions detected by UWF SS-OCTA are clearly visualized, aiding in the diagnosis of Stickler syndrome.[24] In clinical practice, we observed that some preretinal vitreous strands remained nearly fixed in their positions and did not always appear within areas of retinal degeneration. Taken together with vitreous anchoring and traction (Figs 1, 2, and 5), we propose that these fixed vitreous strands, which may coexist with or be independent of degenerative areas, represent critical sites predisposing to retinal breaks and detachment.

The aforementioned findings refute that retinal traction in Stickler syndrome is confined to the peripheral retina.[20] Furthermore, they explain the RD in some patients despite having received prophylactic treatment (360° encircling cryotherapy or laser covering ora serrata to the equator),

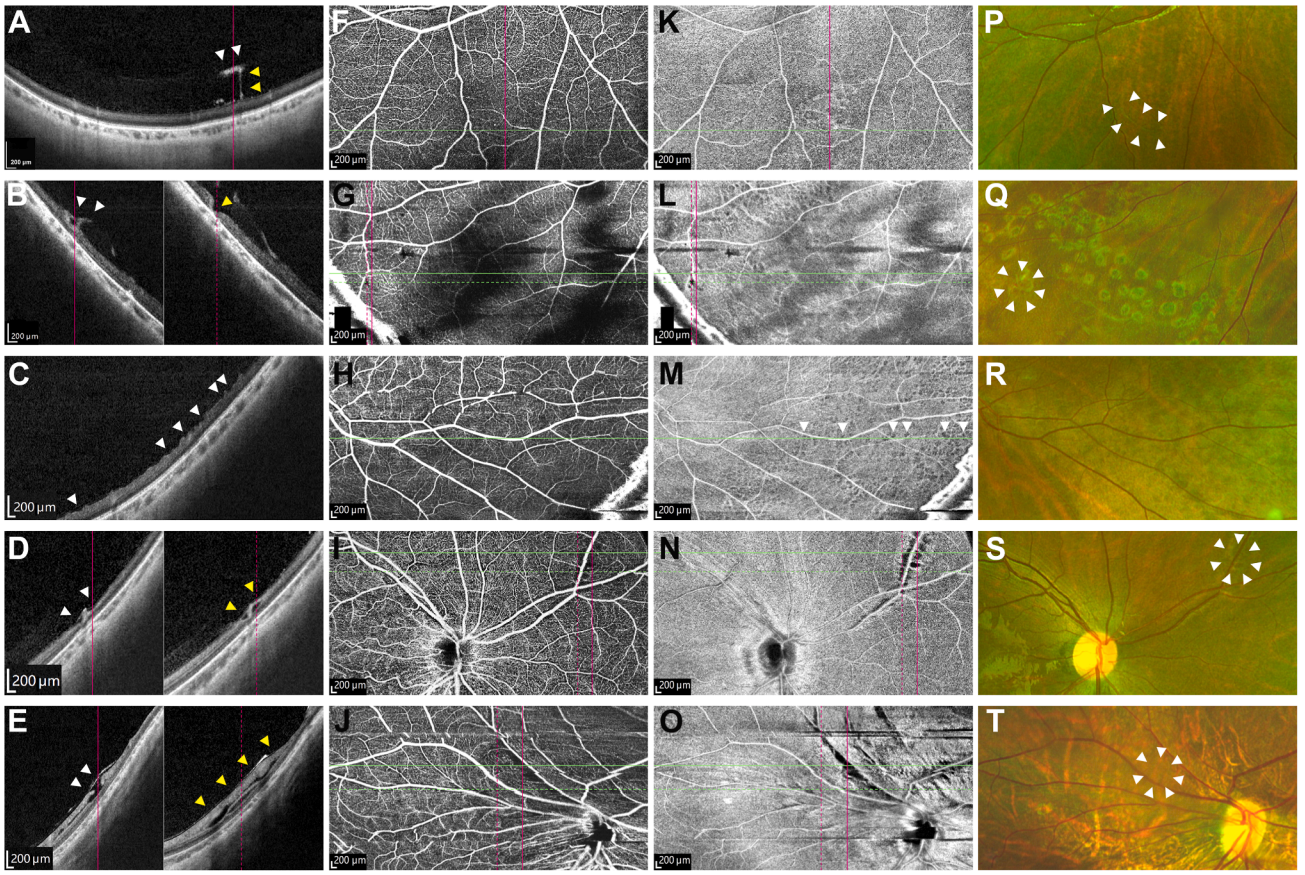


Figure 5. Multimodal images of fundus features in patients with Stickler syndrome. **A**–**E**, Transverse scan images, with purple longitudinal lines showing the scan positions. **F**–**J**, Blood flow images of the superficial capillary plexus, with green transverse lines and purple longitudinal lines showing the scan positions. **K**–**O**, En face images of superficial capillary plexus. **P**–**T,** Scanning laser ophthalmoscopy images, with purple circles showing the lesions. **A**, Representative image of vitreous fiber strand opacity (white arrowheads) with vitreous anchoring (yellow arrowheads). **P**, Scanning laser ophthalmoscopy image showing the vitreous fiber strand opacity (white arrowheads) in (**A**). **B**, Representative images of vitreoretinal traction (white arrowheads) and retinal breaks (yellow arrowheads). **Q**, Scanning laser ophthalmoscopy image showing microholes (white arrowheads). **C**, Representative image of a pitted retinal surface (the depressions marked by white arrowheads). **M**, En face image showing the moonlike retinal surface (the small pits of the scan position marked by white arrowheads). **D**, Representative image of perivascular cavitation (yellow arrowheads) with inner retinal atrophy (white arrowheads). **S**, Scanning laser ophthalmoscopy image showing inconspicuous abnormality in the retinal appearance (white arrowheads). **E**, Representative image of retinal break (white arrowheads) and intraretinal cystoid spaces (yellow arrowheads). **N** and **O**, En face images delineating the full contour of perivascular lesions. **T**, Scanning laser ophthalmoscopy image showing the position of a retinal break and intraretinal cystoid spaces in (**E**; white arrowheads).

with failure rates of 7% to 36%.[25–27] Therefore, defining the optimal extent of prophylaxis remains a major challenge in reducing the high incidence of RD in Stickler syndrome (lifetime risk up to 65%[28]). This study provides an important insight: by identifying all sites of vitreous anchoring using UWF SS-OCTA, it may enable determination of minimal area requiring prophylaxis (including degeneration if necessary). This approach would not only reduce the workload for clinicians but also improve the outcomes (by reducing the failure rate) and decrease complications in prophylactic treatment.[29]

There are also other findings. The "pitted retinal surface" observed in patients with Stickler syndrome had a detection rate up to 75%, which may be a congenital developmental anomaly and serve as one of the imaging biomarkers (Figs 3 and 5). Foveal hypoplasia is well recognized in Stickler syndrome, and its incidence reported previously is similar to that observed in the current study.[30] This study further revealed that among patients with FH, approximately half exhibited FAZ absence, and about one-third of the latter showed a fingerprint sign (indicating FH[31]) (Table 1). Besides, the presence of FAZ exhibits a significant negative correlation with FH ($\rho = -0.56$; $P = 0.007$). The 3 macular features can be clearly visualized using UWF SS-OCTA and can be used as biomarkers for assessing the severity of FH.

Ultra-widefield SS-OCTA really offers distinct advantages in Stickler syndrome. As a disease characterized by early-onset high myopia, Stickler syndrome often presents with tessellated fundus that may obscure typical retinal changes, making early recognition difficult.[32] However, multimodal imaging with UWF SS-OCTA eliminates this interference and clearly visualizes a variety of fundus phenotypes (Fig 5), helping in severity assessment and risk

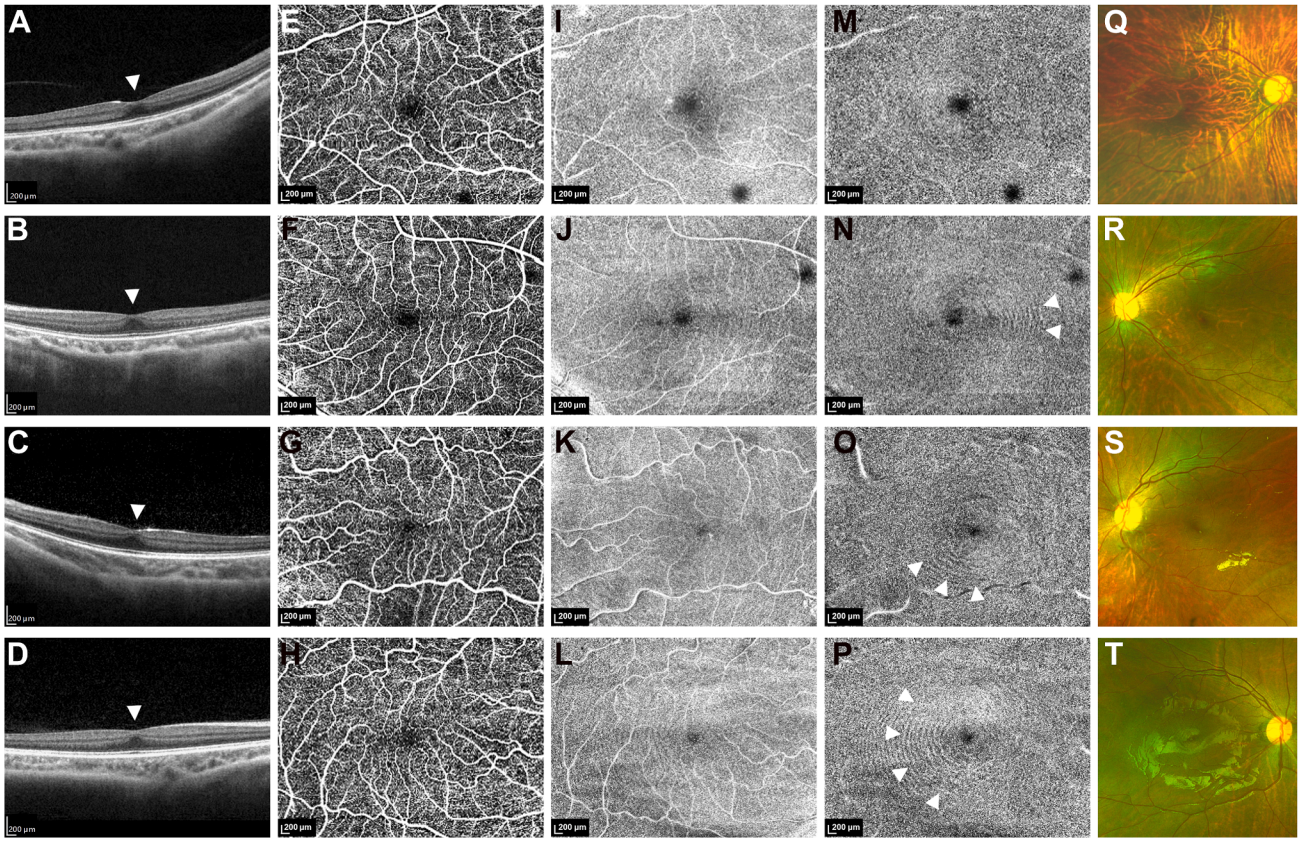


Figure 6. Multimodal images of the macula in patients with Stickler syndrome. **A**–**D**, Transverse scan images of maculas (white arrowheads) with foveal hypoplasia. **E**–**H**, Blood flow images of the entire retina slab showing relatively small foveal avascular zones (**E**, **F**) and foveal avascular zone absence (**G**, **H**). **I**–**L**, En face images of superficial capillary plexus. **M**–**P**, En face images of the deep capillary plexus exhibiting a gradually remarkable fingerprint sign (white arrowheads). **Q**–**T**, Scanning laser ophthalmoscopy images.

Table 2. Correlation Analysis between Fundus Features and Basic Clinical Characteristics in Patients with Stickler Syndrome

Parameters	Age[†]	Gender[‡]	SE[†]	AL[§]
Vitreous features				
Vitreous liquefaction pockets	−0.27 (0.20)	0.21 (0.38)	0.07 (0.73)	−0.10 (0.62)
Vitreous lamellation	0.15 (0.48)	0.12 (0.65)	0.18 (0.39)	−0.16 (0.45)
Vitreous opacities	NA	NA	NA	NA
Punctate dense granules	0.58 (0.005)*	−0.36 (0.22)	0.27 (0.22)	−0.07 (0.76)
Vitreoretinal features				
Vitreous anchoring	0.58 (0.005)*	−0.36 (0.22)	0.27 (0.22)	−0.07 (0.76)
Vitreoretinal traction	0.41 (0.054)	0.20 (0.42)	−0.01 (0.95)	0.17 (0.43)
Retinal degeneration	−0.31 (0.15)	−0.19 (1.00)	0.13 (0.56)	0.09 (0.68)
Retinal features				
Pitted retinal surface	0.62 (0.002)*	−0.01 (1.00)	−0.34 (0.12)	0.44 (0.04)*
PCIRA	−0.57 (0.009)*	0.14 (1.00)	0.10 (0.68)	−0.09 (0.70)
Intraretinal cystoid spaces	0.42 (0.054)	0.04 (1.00)	−0.15 (0.49)	0.21 (0.36)
Retinal breaks	−0.02 (0.94)	−0.06 (1.00)	−0.23 (0.28)	0.17 (0.45)
RD	0.24 (0.27)	0.34 (0.23)	−0.31 (0.15)	0.54 (0.008)*
Macular features				
FH	−0.03 (0.90)	0.19 (0.64)	−0.08 (0.72)	0.24 (0.27)
FAZ absence	0.56 (0.007)*	−0.27 (0.39)	−0.03 (0.90)	−0.26 (0.25)
Fingerprint sign	−0.02 (0.93)	0.38 (0.22)	0.16 (0.44)	−0.18 (0.40)

Data are presented as Spearman correlation coefficient (ρ) and the corresponding 2-sided *P* value in parentheses below for each cell. AL = axial length; FAZ = foveal avascular zone; FH = foveal hypoplasia; NA = not available; PCIRA = perivascular cavitation with inner retinal atrophy; RD = retinal detachment; SE = spherical equivalent.
*$P < 0.05$.
[†]Spearman rank-order correlation.
[‡]Φ coefficient.
[§]Point-biserial correlation.

stratification. Moreover, it enables both transverse and longitudinal serial scanning of retina, facilitating the detection of tiny lesions. Except for those mentioned earlier, the fundus findings in Stickler syndrome, particularly the vitreoretinal features, also guide surgical decision-making: compared with scleral buckling alone, vitrectomy or combined surgeries may yield better long-term outcomes.

This study has several limitations. First, the sample size of this study is relatively small because Stickler syndrome is a rare disease. Despite the small number of cases, we performed comprehensive multimodal imaging evaluation. The novel imaging biomarkers and pathogenic mechanisms identified in this study provide new insights for the diagnosis, treatment, and prophylaxis of this potentially blinding disease. These findings warrant attention from ophthalmologists worldwide. Second, this study did not include a separate normal control group because we aimed to preliminarily characterize the fundus features in patients with Stickler syndrome, and the fundus appearance of normal individuals with myopia is well known, and these abnormalities are very uncommon in normal individuals.[33] Finally, although we propose that vitreous anchoring may serve as a key underlying mechanism for retinal breaks and detachment, further prospective studies are still needed to validate the causality and to test the efficacy of targeted prophylaxis.

Conclusion

This study used UWF SS-OCTA to systematically characterize fundus phenotypes of Stickler syndrome. Among the 15 identified features, vitreous abnormalities were the most prevalent. We provide in vivo imaging evidence that vitreous anchoring may be a key trigger for retinal breaks and detachment in Stickler syndrome, likely acting through vitreoretinal traction. Its concealment beneath the vitreous fibrous strands may offer a potential theoretical basis for improving targeted prophylaxis and treatment. The other features, such as a pitted retinal surface and FH-related macular signs, may serve as imaging biomarkers, aiding early and efficient diagnosis or risk stratification.

Acknowledgments

The authors appreciate the Shenzhen Eye Hospital Medical Ethics Committee for approving the conduct of this study (2025KYPJ208).

Footnotes and Disclosures

Originally received: June 5, 2026.
Final revision: August 27, 2026.
Accepted: August 27, 2026.
Available online: September 3, 2026. Manuscript no.: XOPS-D-26-00580R2.

[1] Shenzhen Eye Hospital, Jinan University, China.

[2] Shenzhen Eye Hospital, Shenzhen Eye Medical Center, Southern Medical University, Shenzhen, China.

[3] Department of Ophthalmology, Center for Preventive Ophthalmology and Biostatistics, Perelman School of Medicine, University of Pennsylvania, Philadelphia, Pennsylvania.

*Y.H., K.C., and Z.W. contributed equally as co-first authors.

†X.Z. and G.Z. contributed equally.

Disclosure(s):

All authors have completed and submitted the ICMJE disclosures form.

The authors have no proprietary or commercial interest in any materials discussed in this article.

This work was supported by the National Natural Science Foundation of China (grants no.: 82271103, 82401315, 82401272, 82301269, and 82671377); the Shenzhen Medical Research Fund (grants no.: C2501034, A2403020, C2301005, and D250403004); the Shenzhen Science and Technology Program (grants no.: JCYJ20240813152703005, JCYJ20250604184009011, and ZDYJ20251211141301002); the Guangdong Basic and Applied Basic Research Foundation (grant no.: 2026A1515012558); the Guangdong Provincial Medical Science and Technology Research Fund (grant no.: B2025169); and the Sanming Project of Medicine in Shenzhen (grant no.: SZSM202311018).

Data Availability: Due to national ethical restrictions, the data used and analyzed in this study are not publicly available. With publication, deidentified data collected in this study (excluding additional documents such as study protocol and informed consent form) can be requested from the lead corresponding author, G.M.Z., via email for academic purposes. Such requests will be subject to approval by the Ethics Committee of Shenzhen Eye Hospital and the execution of a signed bilateral collaboration agreement and a data access agreement with the requesting party.

HUMAN SUBJECTS: Human subjects were included in this study. This is a cohort study conducted at Shenzhen Eye Hospital. The study protocol was approved by the Medical Ethics Committee of Shenzhen Eye Hospital (2025KYPJ208) and informed consent was obtained from the parents or legal guardians of all participants prior to study initiation. This study adhered to the Declaration of Helsinki.

No animal subjects were used in this study.

Author Contributions:

Conception and design: Hu, Cui, Wu, Zhao, G. Zhang

Data collection: Hu, Cui, Wu, Li, S. Zhang, Luo, He, Cheng, Ying, Zhao

Analysis and interpretation: Hu, Cui, Wu, Li, S. Zhang, Zhao, G. Zhang

Obtained funding: Cui, Wu, Zhao, G. Zhang

Overall responsibility: Hu, Cui, Wu, Li, S. Zhang, Luo, He, Cheng, Ying, Zhao, G. Zhang

Abbreviations and Acronyms:
AL = axial length; **FAZ** = foveal avascular zone; **FH** = foveal hypoplasia; **PCIRA** = perivascular cavitation with inner retinal atrophy; **RD** = retinal detachment; **SLO** = scanning laser ophthalmoscopy; **UWF SS-OCTA** = ultra-widefield swept-source OCT angiography.

Keywords:
Fundus features, Multimodal imaging, Retinal detachment, Stickler syndrome, Ultra-widefield swept-source OCT angiography.

Correspondence:
Xinyu Zhao and Guoming Zhang, Shenzhen Eye Hospital, Shenzhen Eye Medical Center, Southern Medical University, 18 Zetian Rd, Futian, Shenzhen, 518040, China. E-mail: xiny.zhao04@gmail.com; zhang-guoming@163.com.

References

1. Orphanet. Stickler syndrome. *ORPHANET: Maladies Rares Medicaments Orphelins*. INSERM; 2021. v. 2026.
2. Constant A, Daruich A, Bernabei F, et al. Genotype-phenotype correlations of COL2A1 and COL11A1 patients. *Am J Ophthalmol*. 2026;281:17−24.
3. Alshahrani ST, Ghazi NG, Al-Rashaed S. Rhegmatogenous retinal detachments associated to Stickler syndrome in a tertiary eye care center in Saudi Arabia. *Clin Ophthalmol*. 2016;10:1−6.
4. Fernández-Pérez JJ, Mascaraque-Ruiz P, Martín Gómez C, et al. Quality of life in children and adolescents with Stickler syndrome in Spain. *Children (Basel)*. 2022;9:1255.
5. Taylor K, Su M, Richards Z, et al. Outcomes in retinal detachment repair and laser prophylaxis for syndromes with optically empty vitreous. *Ophthalmol Retina*. 2023;7:848−856.
6. Burdová M, Štěpánková J, Pourová RK, et al. Long-term anatomical and functional outcomes of surgical treatment of retinal complications in children and adolescents with Stickler syndrome between 2004 and 2021. *Graefes Arch Clin Exp Ophthalmol*. 2023;261:1723−1729.
7. Smith JM, Ward LT, Townsend JH, et al. Rhegmatogenous retinal detachment in children: clinical factors predictive of successful surgical repair. *Ophthalmology*. 2019;126:1263−1270.
8. Maghsoudi D, Nixon TR, Martin H, et al. Retinal detachment in Type IX collagen recessive Stickler syndrome. *Eye (Lond)*. 2025;39:133−138.
9. Snead MP, McNinch AM, Poulson AV, et al. Stickler syndrome, ocular-only variants and a key diagnostic role for the ophthalmologist. *Eye (Lond)*. 2011;25:1389−1400.
10. Lee AR, Bhagat N, Hromas A, et al. Stickler Syndrome. *EyeWiki*. American Academy of Ophthalmology; 2022. v. 2026.
11. Chen X, Ju Y, Gao F, et al. Rhegmatogenous Retinal Detachment Secondary to Type I Stickler Syndrome: Diagnosis, Treatment and Long-Term Outcomes. *Genes (Basel)*. 2024;15:1455.
12. Zheng F, Deng X, Zhang Q, et al. Advances in swept-source optical coherence tomography and optical coherence tomography angiography. *Adv Ophthalmol Pract Res*. 2023;3:67−79.
13. Zhao X, Wu Z, Liu Y, et al. Eyecare-cloud: an innovative electronic medical record cloud platform for pediatric research and clinical care. *EPMA J*. 2024;15:501−510.
14. Carpenter CM, MacLachlan AG, Kwun CY, et al. Relative risk of retinal detachment in COL2A1 compared with COL11A1 Stickler syndrome: an individual patient data meta-analysis. *Ophthalmol Retina*. 2026;10:194−203.
15. Drackley A, Ralay Ranaivo H, Allegretti V, et al. Ophthalmic manifestations in a diverse pediatric population with type I and type II Stickler syndrome. *Ophthalmol Retina*. 2025;9:690−698.
16. Koh K, Tuuminen R, Jeon S. Ultra-widefield-guided swept-source OCT findings of peripheral vitreoretinal abnormality in young myopes. *Ophthalmology*. 2024;131:434−444.
17. Nagashima T, Akiyama H, Nakamura K, et al. Posterior precortical vitreous pocket in Stickler syndrome: a report of two cases. *Cureus*. 2024;16:e59633. https://doi.org/10.7759/cureus.59633.
18. Chen KC, Jung JJ, Engelbert M. Giant premacular bursa: a novel finding of the posterior vitreous in two patients with Stickler syndrome type 1 revealed by swept-source optical coherence tomography. *Graefes Arch Clin Exp Ophthalmol*. 2016;254:591−593.
19. Ghoraba HH, Sears J, Traboulsi EI. Hereditary vitreoretinopathies: molecular diagnosis, clinical presentation and management. *Clin Exp Ophthalmol*. 2025;53:281−291.
20. Morris RE, Kuhn F, Sipos T. Preventing retinal detachment: where are we? Implications from Stickler syndrome. *Clin Ophthalmol*. 2022;16:4315−4321.
21. Xiong J, Tran T, Waldstein SM, Fung AT. A review of rhegmatogenous retinal detachment: past, present and future. *Wien Med Wochenschr*. 2025;175:186−202.
22. MacRae ME, Patel DV, Richards AJ, et al. Type 1 Stickler syndrome: a histological and ultrastructural study of an untreated globe. *Eye (Lond)*. 2006;20:1061−1067.
23. Alsharif FR, Alwisi N, Irshaidat S, et al. Rhegmatogenous retinal detachment in Stickler syndrome: a systematic review and meta-analysis. *Ophthalmol Retina*. 2026;10:420−441.
24. Parma ES, Körkkö J, Hagler WS, Ala-Kokko L. Radial perivascular retinal degeneration: a key to the clinical diagnosis of an ocular variant of Stickler syndrome with minimal or no systemic manifestations. *Am J Ophthalmol*. 2002;134:728−734.
25. Alexander P, Fincham GS, Brown S, et al. Cambridge prophylactic protocol, retinal detachment, and Stickler syndrome. *N Engl J Med*. 2023;388:1337−1339.
26. Khanna S, Rodriguez SH, Blair MA, et al. Laser prophylaxis in patients with Stickler syndrome. *Ophthalmol Retina*. 2022;6:263−267.
27. Fincham GS, Pasea L, Carroll C, et al. Prevention of retinal detachment in Stickler syndrome: the Cambridge prophylactic cryotherapy protocol. *Ophthalmology*. 2014;121:1588−1597.
28. Morris RE, Kuhn F, Richardson C. Preventing retinal detachment: the encircling laser retinopexy technique. *Clin Ophthalmol*. 2023;17:1505−1513.
29. Dos Anjos Filho VM, Gaban NG, Hira S, et al. Comparative outcomes of focal laser versus 360-degree laser in vitrectomy for retinal detachment: a systematic review and meta-analysis. *Int J Retina Vitreous*. 2026;12:27.
30. Matsushita I, Nagata T, Hayashi T, et al. Foveal hypoplasia in patients with Stickler syndrome. *Ophthalmology*. 2017;124:896−902.
31. Ramtohul P, Comet A, Denis D. Multimodal imaging correlation of the concentric macular rings sign in foveal hypoplasia: a distinctive Henle fiber layer geometry. *Ophthalmol Retina*. 2020;4:946−953.
32. Zhou L, Xiao X, Li S, et al. Phenotypic characterization of patients with early-onset high myopia due to mutations in COL2A1 or COL11A1: why not Stickler syndrome? *Mol Vis*. 2018;24:560−573.
33. Si Y, Pang K, Song Y, et al. Observation of structural and vascular features of retina and choroid in myopia using ultra-widefield SS-OCTA. *BMC Ophthalmol*. 2024;24:208.